Exploration Geophysics

ISSN: 0812-3985 (Print) 1834-7533 (Online) Journal homepage: https://www.tandfonline.com/loi/texg20

3D CSAMT modelling in anisotropic media using edge-based finite-element method

Guoli He, Tiaojie Xiao, Yun Wang & Guangjie Wang

To cite this article: Guoli He, Tiaojie Xiao, Yun Wang & Guangjie Wang (2019): 3D CSAMT modelling in anisotropic media using edge-based finite-element method, Exploration Geophysics, DOI: 10.1080/08123985.2019.1565914

To link to this article: https://doi.org/10.1080/08123985.2019.1565914

Published online: 30 Jan 2019.

EXPLORATION GEOPHYSICS
https://doi.org/10.1080/08123985.2019.1565914

Taylor & Francis
Taylor & Francis Group

3D CSAMT modelling in anisotropic media using edge-based finite-element method

Guoli He[a,c], Tiaojie Xiao[b,c], Yun Wang[b] and Guangjie Wang[a,c]

[a]Institute of Geology and Geophysics, Chinese Academy of Sciences, Beijing, China; [b]Institute of Geochemistry, Chinese Academy of Sciences, Guiyang, China; [c]University of Chinese Academy of Sciences, Beijing, China

ABSTRACT

Controlled-source audio-frequency magnetotellurics (CSAMT) is an important geophysical technique. Numerous studies have shown that the electrical anisotropy in the Earth cannot be ignored because it would probably lead to misinterpretations of electromagnetic data. It is necessary and meaningful to study CSAMT responses in three-dimensional (3D) electrical anisotropic media; therefore, we have developed an edge-based finite element method for 3D CSAMT forward modelling in generalised anisotropic media. The total electric field in this approach is decomposed into a primary electric field and a secondary electric field, and the Galerkin weighted residuals method is adopted to obtain the variational equation. The accuracy of this algorithm was initially validated by comparing solutions with those obtained in previous work on a 3D arbitrary anisotropic model. We then studied the responses of an oblique source as well as equatorial and axial configurations and the tensor source for anomalies with different Euler's angles. Several meaningful conclusions can be derived from this work and a synthetic model is developed; the results also confirm the validity of previous conclusions. This study shows that a tensor source is necessary for a CSAMT survey in 3D anisotropic media, and the anisotropic parameters of anomalies have complex and significant influences on CSAMT responses.

ARTICLE HISTORY
Received 10 June 2018
Accepted 5 November 2018

KEYWORDS
CSAMT; anisotropy; modelling; three-dimensional; finite element

Introduction

Controlled-source audio-frequency magnetotellurics (CSAMT) has proved a highly successful geophysical technique and is now widely used across many areas including mineral resource surveys and oil and gas exploration (Boerner et al. 1993; Wannamaker 1997; Unsworth et al. 2000; Hu et al. 2013; Younis et al. 2015; Pedrera et al. 2016; Wang et al. 2017b). Numerous studies in this area have been carried out including in one-dimensional (1D) and two-dimensional (2D) media (Routh and Oldenburg 1999; Lu et al. 1999; Di et al. 2004; Fu et al. 2013; Wang et al. 2015). In early work, Lin et al. (2012) developed an algorithm for three-dimensional (3D) CSAMT forward modelling based on the finite difference (FD) method and presented a conjugate gradient approach to invert the resultant data. Later, McMillan and Oldenburg (2014) developed a Gauss–Newton inversion method that was able to process realistic 3D CSAMT data, while Hu et al. (2015) presented 3D tensor CSAMT forward modelling using an edge-based finite element (FE) method. Wang et al. (2017a) then developed a 3D tensor CSAMT inversion using the limited-memory Broyden–Fletcher–Goldfarb–Shanno (LBFGS) method with full impedance data; however, this study revealed that incorrect results are obtained if a magnetotelluric (MT) inversion method is used to invert the data of tensor CSAMT. All these studies are based on electrically isotropic theory, although it is well known that the earth is actually electrically anisotropic (Evans et al. 2005; Kong et al. 2018), and numerous studies have been carried out in relation to controlled-source electromagnetic modelling and inversion in anisotropic media, especially in the marine realm (Li and Pedersen 1992; Kong et al. 2008; Key 2009; Newman et al. 2010; Puzyrev et al. 2013; Cai et al. 2014; Yin et al. 2014; Jakobsen and Tveit 2018; Wang et al. 2018). In the specific case of CSAMT, Wang and Tan (2017) presented a 3D tensor CSAMT modelling algorithm that applies the FD method in axial conductive anisotropic media, and analysed the responses of several configurations. However, they did not take generalised anisotropy into consideration and so Wang et al. (2017c) studied the inversion of CSAMT using the LBFGS method in an axial anisotropic case. The results of this study suggest that isotropic inversion introduces errors into anisotropic data interpretation.

The FE method has been applied widely to problems in electromagnetic (EM) modelling (Ren et al. 2013; Li et al. 2016). In terms of the nodal FE method specifically, unknown components are expressed as a linear combination of scalar basis functions; thus, one vertex is shared by several cells and components are located at

CONTACT Tiaojie Xiao xiaotiaojie16@mails.ucas.ac.cn Institute of Geochemistry, Chinese Academy of Sciences, Guiyang 550081, China

nodes such that each is continuous with the next. This means that the tangential component of the electric field remains continuous even though the conductivity is discontinuous, which violates the discontinuity condition required for the normal component of the electric field at different conductivity contrasts (Ansari and Farquharson 2014). In addition, because unknown components can vary in 3D, the approximate field cannot satisfy the divergence-free condition in a source-free region and it is necessary to contrast this with the fact that the true electric field should be divergence-free in each cell where there is no current source or charge (Farquharson and Miensopust 2011). An edge-based FE approach was adopted here because it enabled us to completely overcome the disadvantages inherent in the node-based FE method (Jin 2002; Cai et al. 2017). The final derived system of equations also comprises a large and sparse matrix equation; this is solved here using a bi-conjugate gradient stabilised (Bi-CGSTAB) solver with a symmetric successive over-relaxation (SSOR) preconditioner. Our aim is to study CSAMT responses with a range of different source configurations.

CSAMT modelling in 3D anisotropic media

The problem formulation

We assume a harmonic time dependence of $e^{-i\omega t}$ and neglect displacement currents because $\sigma >> \omega\varepsilon$ for the frequencies of CSAMT. Magnetic permeability is assumed to be equal to the value in air (μ_0). Equations (1) and (2) can therefore be obtained from Maxwell's equations, as follows:

$$\nabla \times \mathbf{E} = i\omega\mu_0\mathbf{H}, \tag{1}$$

and

$$\nabla \times \mathbf{H} = \mathbf{J}_s + \hat{\sigma}\mathbf{E}. \tag{2}$$

In these expressions, **E** denotes the electric field, **H** is the magnetic field, i is $\sqrt{-1}$, ω is the angular frequency, $\hat{\sigma}$ is conductivity, a tensor in electrical anisotropic media and $\mathbf{J}_s$ is the source current distribution. The tensor conductivity, $\hat{\sigma}$, can be obtained via two methods (Yin 2000; Pek and Santos 2002), the latter of which is adopted where the conductivity, $\hat{\sigma}$, is defined by three Euler's angles (α_S, α_D and α_L) and three axial conductivities (σ_x, σ_y and σ_z) (following Pek and Santos 2002).

Thus, based on Equations (1) and (2), Equation (3) can be obtained, as follows:

$$\nabla \times \nabla \times \mathbf{E} - i\omega\mu_0\hat{\sigma}\mathbf{E} = i\omega\mu_0\mathbf{J}_s. \tag{3}$$

In follows that the total electric field, **E**, can be decomposed into the primary electric field and the secondary electric field (Wang and Tan 2017), as follows:

$$\mathbf{E} = \mathbf{E}^{\mathrm{P}} + \mathbf{E}^{\mathrm{S}}. \tag{4}$$

It is therefore also the case that Equation (3) can be revised, as follows:

$$\nabla \times \nabla \times \mathbf{E}^{\mathrm{S}} - i\omega\mu_0\hat{\sigma}\mathbf{E}^{\mathrm{S}} = i\omega\mu_0(\hat{\sigma} - \hat{\sigma}_{\mathrm{P}})\mathbf{E}^{\mathrm{P}}. \tag{5}$$

In this expression, $\hat{\sigma}_{\mathrm{P}}$ is the background conductivity, $\mathbf{E}^{\mathrm{S}}$ is the secondary electric field and $\mathbf{E}^{\mathrm{P}}$ is the primary electric field. In this paper, Dipole1D (Key 2009) is used to calculate the primary electric field for an isotropic background. In anisotropic media, the conductivity is a tensor as follows:

$$\hat{\sigma} = \begin{pmatrix} \sigma_{xx} & \sigma_{xy} & \sigma_{xz} \\ \sigma_{yx} & \sigma_{yy} & \sigma_{yz} \\ \sigma_{zx} & \sigma_{zy} & \sigma_{zz} \end{pmatrix}. \tag{6}$$

The conductivity tensor can be defined by two methods (Yin 2000; Pek and Santos 2002). The latter in which the conductivity tensor can be expressed by three principle conductivities (σ_x, σ_y and σ_z) and three Euler's angles (α_S, α_D and α_L) is adopted here, as shown in Figure 1,

FE analysis

An edge-based FE method is adopted in this analysis (Figure 2).

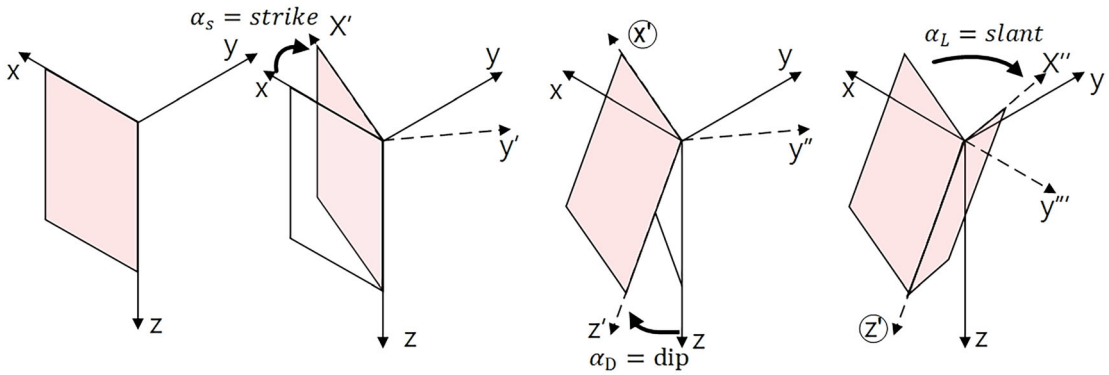

Figure 1. Basic anisotropy parameters (Pek and Santos 2002).

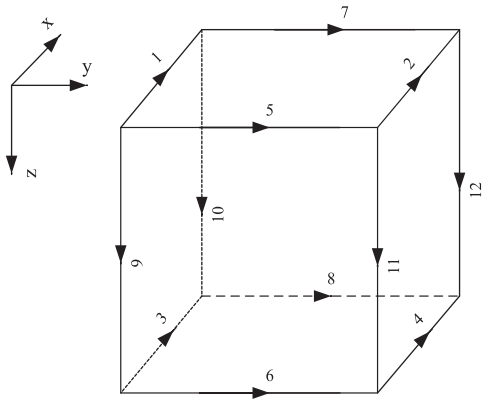

Figure 2. One hexahedral element.

We apply a Whitney vector basis; thus, for a given element (Jin 2002):

$$\mathbf{E}_{x,e} = \sum_{i=1}^{4} \mathbf{N}_{x,i} E_{x,i}, \mathbf{E}_{y,e} = \sum_{j=1}^{4} \mathbf{N}_{y,j} E_{y,j}, \mathbf{E}_{z,e} = \sum_{k=1}^{4} \mathbf{N}_{z,k} E_{z,k}. \tag{7}$$

The Galerkin method (Xu 1994) was then applied to obtain the variational equation. Multiplying both sides of Equation (5) by the Whitney vector basis (**N**), and considering Equation (5), the vector identity (Equation 8) and divergence theorem (Equation 9) can be fused, as follows:

$$\nabla \cdot (\mathbf{A} \times \mathbf{B}) = (\nabla \times \mathbf{A}) \cdot \mathbf{B} - \mathbf{A} \cdot (\nabla \times \mathbf{B}), \tag{8}$$

and

$$\int_v \nabla \cdot \mathbf{A} dv = \oint_\Gamma \mathbf{A} \cdot \mathbf{n} d\Gamma. \tag{9}$$

On this basis, Equation (10) can be obtained, as follows:

$$\int_V \nabla \mathbf{N} \cdot \nabla \times \mathbf{E}^{\mathrm{S}} \mathrm{d}v - \int_V i\omega\mu_0 \tilde{\sigma} \mathbf{N} \cdot \mathbf{E}^{\mathrm{S}} \mathrm{d}v - \int_V i\omega\mu_0 \tilde{\sigma}^a \mathbf{N} \cdot \mathbf{E}^{\mathrm{P}} \mathrm{d}v = 0. \tag{10}$$

In this expression, $\tilde{\sigma}^{\mathrm{a}} = \tilde{\sigma} - \tilde{\sigma}^P$. Calculating each integral in Equation (10) for each element, the following matrix expression can be obtained,

$$[\mathbf{K}_e^1 - \mathbf{K}_e^2]\mathbf{E}_e^{\mathrm{S}} = [\mathbf{K}_e^3]\mathbf{E}_e^{\mathrm{P}} \tag{11}$$

In this expression, $\mathbf{K}_e^1$, $\mathbf{K}_e^2$ and $\mathbf{K}_e^3$ are 12×12 matrices, as discussed in more detail in Appendix A.

Assuming the outer boundaries are far enough from the anomalies, the secondary electric fields can be set to be zero at these margins. This means that we can assemble Equation (11) to encompass all elements and add Dirichlet boundary conditions such that Equation (12) can be derived, as follows:

$$\mathbf{A}\mathbf{x} = \mathbf{b}. \tag{12}$$

The secondary electric field can then be obtained after solving Equation (12).

Apparent resistivity and phase

The three types of sources used in this analysis are shown in Figure 3: (a) an equatorial configuration (Tx) along the *x*-axis, (b) an axial configuration (Ty) along the *y*-axis, and (c) a tensor source that consists of two oblique single sources.

Once EM fields are obtained, the apparent resistivity and phase can be calculated (Wang and Tan 2017). In the case of the Tx source, both E_x and H_y are observed, and the apparent resistivity and phase can be calculated using Equation (13), as follows:

$$\rho_{xy} = \frac{1}{\omega\mu_0}\left|\frac{E_x}{H_y}\right|^2 = \frac{1}{\omega\mu_0}|Z_{xy}|^2, \phi_{xy} = \arctan\left|\frac{\mathrm{Im}(Z_{xy})}{\mathrm{Re}(Z_{xy})}\right|. \tag{13}$$

In the case of the Ty source, both E_y and H_x are observed, and the apparent resistivity and phase can be calculated using Equation (14), as follows:

$$\rho_{yx} = \frac{1}{\omega\mu_0}\left|\frac{E_y}{H_x}\right|^2 = \frac{1}{\omega\mu_0}|Z_{yx}|^2, \phi_{yx} = \arctan\left|\frac{\mathrm{Im}(Z_{yx})}{\mathrm{Re}(Z_{yx})}\right|. \tag{14}$$

In the case of the tensor source, E_x, E_y, H_x and H_y of two single sources (source 1 and source 2) were observed. Impedance can be obtained using Equation

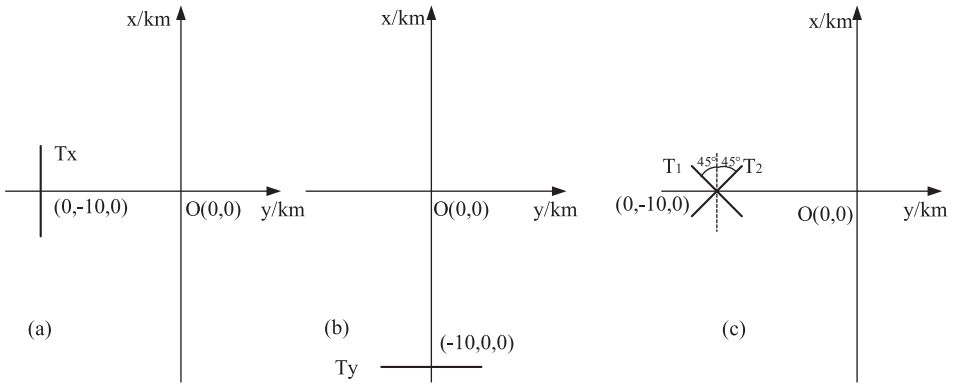

Figure 3. The three types of sources used in this analysis: (a) equatorial configuration (Tx); (b) axial configuration (Ty); (c) tensor source.

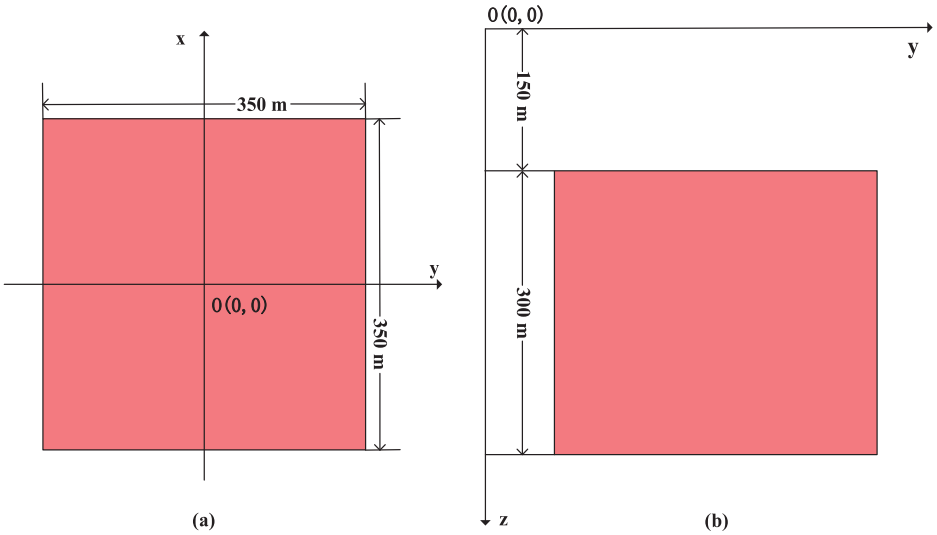

Figure 4. The test model: (a) plan view; (b) section view.

(15), and the apparent resistivity and phase can be obtained by Equation (16), as follows:

$$Z_{xx} = \frac{E_{x1}H_{y2} - E_{x2}H_{y1}}{H_{x1}H_{y2} - H_{x2}H_{y1}} \quad Z_{xy} = \frac{E_{x2}H_{x1} - E_{x1}H_{x2}}{H_{x1}H_{y2} - H_{x2}H_{y1}},$$
$$Z_{yx} = \frac{E_{y1}H_{y2} - E_{y2}H_{y1}}{H_{x1}H_{y2} - H_{x2}H_{y1}} \quad Z_{yy} = \frac{E_{y2}H_{x1} - E_{y1}H_{x2}}{H_{x1}H_{y2} - H_{x2}H_{y1}} \tag{15}$$

and

$$\rho_{ij} = \frac{1}{\omega\mu_0}|Z_{ij}|^2, \phi_{ij} = \arctan\left|\frac{\mathrm{Im}(Z_{ij})}{\mathrm{Re}(Z_{ij})}\right| (i = x, y; j = x, y). \tag{16}$$

The centre coordinates of the Tx, Ty and tensor sources were all set at zero, −10,000 m and 1 m. The length was 300 m, and the current was 1 A in all cases.

Accuracy validation

We made comparisons with a 3D CSAMT FD anisotropy code of Wang and Tan (2017) at 100 Hz to validate the accuracy of our approach. This necessitates a 3D model, as shown in Figure 4: the dimensions of the anomaly in this case are 350 m × 350 m × 300 m, its top depth is 150 m, the three principal conductivities are 0.02, 1/30 and 0.1 S/m, and its three Euler's angles are zero. This 3D anomaly was embedded in an isotropic half-space of 0.01 S/m.

The xy- and yx-mode apparent resistivities and phase for these two methods at 100 Hz are illustrated in Figure 5: the first row corresponds to the results for the FE method developed in this paper; the second to the results for the FD method in Wang and Tan (2017) and the third to relative errors; the first column corresponds to the xy-mode apparent resistivity, the second to the yx-mode apparent resistivity, the third to the xy-mode phase and the fourth to the yx-mode phase. The results reveal very close agreement between the two methods because the relative errors are all $<$ 1%. Because our purpose is to verify the accuracy of the algorithm developed in this paper, these results are not analysed in further detail.

The code was written by MATLAB on a computer with an Intel® Core™ i7-4790 3.60 GHz processor, and we solved the system equation using a Bi-CGSTAB solver with a SSOR preconditioner. The grid is 40 × 40 × 41 (in the *x*-, *y*- and *z*-direction respectively). It took 352 and 354 s to solve the two system equations (Ta and Tb). Air is usually represented by a small non-zero conductivity; however, this results in an ill-conditioned system of equations (Mitsuhata and Uchida 2004). Here, the conductivity in air is set at 10^{-10} S/m. The convergence plot of this result is shown in Figure 6, and the data show that a scheme incorporating a Bi-CGSTAB solver with a SSOR preconditioner works well.

Numerical experiments

In this section, single oblique sources with different incline angles are studied first, followed by a simple 3D anisotropic anomaly under different conditions. Finally, a synthetic model is designed, and its responses are analysed.

Single source

Single oblique source

To study the influence of an oblique source, a Tx version with a different incline angle (i.e. from the positive *x*-direction to the positive *y*-direction) and a Ty source with a different incline angle (i.e. from the positive *y*-direction to the negative *x*-direction) were utilised. The model is the same as that shown in Figure 4, its three principal conductivities are 0.04, 0.0025 and 0.01 S/m, the three Euler's angles are all equal to zero, and the isotropic-half space is 0.01 S/m.

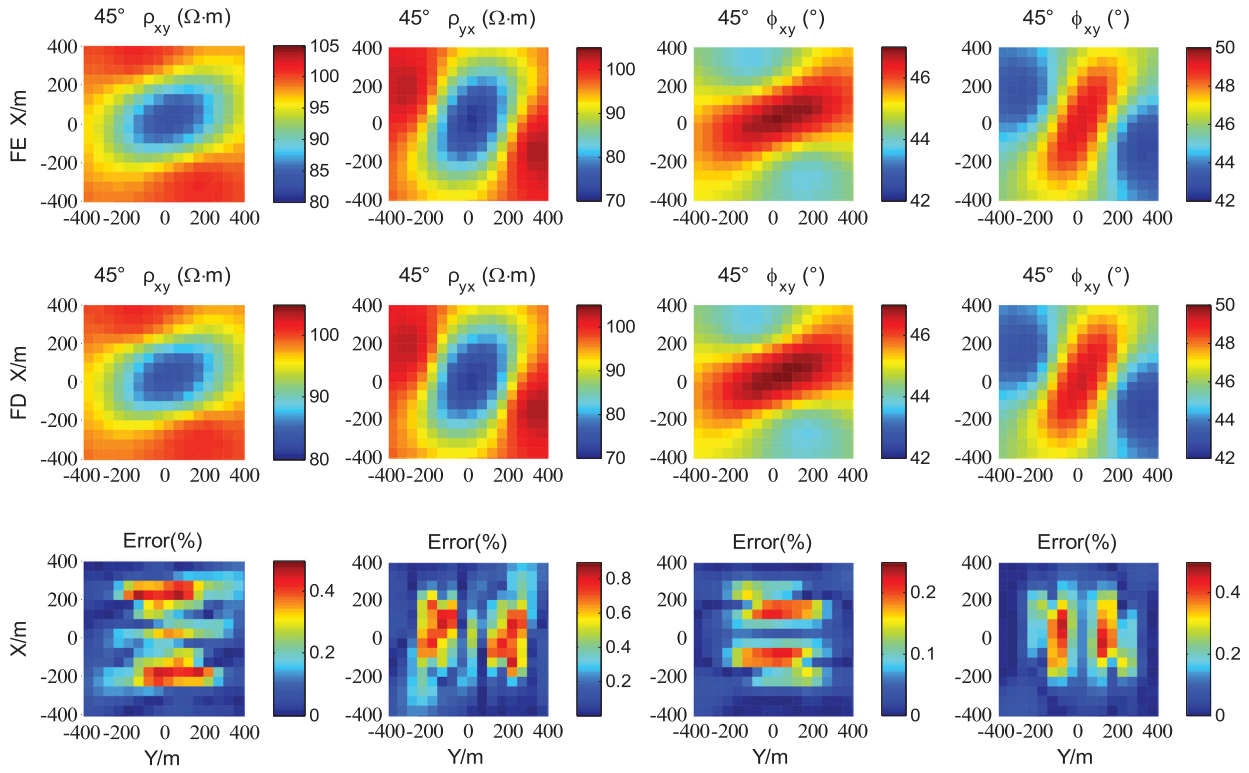

Figure 5. Comparisons between the results of the finite element (FE) and finite difference (FD) methods.

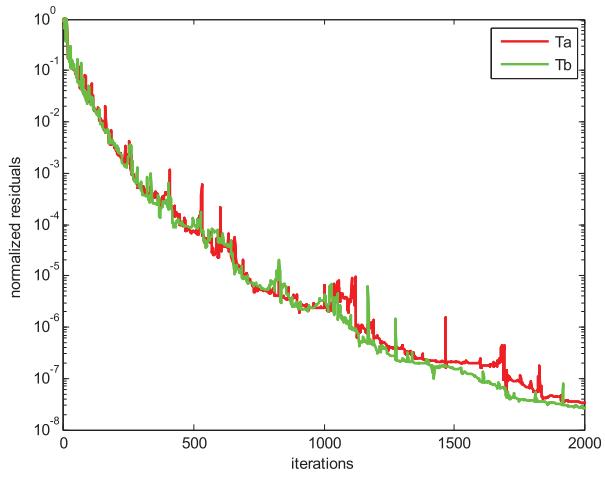

Figure 6. Normalised residuals of the test model. Ta and Tb denote the two single oblique sources of the tensor source.

(1) A single oblique Tx source. We studied another isotropic model for comparison; the conductivity of the 3D anisotropic anomaly was set at 0.04 S/m in the isotropic model. The data presented in Figure 7 show the apparent resistivity of these two models at 100 Hz; the first row corresponds to the anisotropic model and the second to the isotropic model. The first to the fifth columns in this figure correspond to Tx incline angles of −30°, −15°, 0°, 15° and 30° respectively. The distribution of the apparent resistivity changes as the incline angle changes, although this variable exhibits different behaviours for the same incline angle in for anisotropic and isotropic models. The induction mechanism is very complex because the secondary field depends on both the primary field and the media. For instance, the secondary field E_z is influenced by the 3D anomaly and the three components of the primary field. Since H_y can be expressed by E_x and E_z (Xiao et al. 2018), the xy-mode apparent resistivities here depend on E_x and E_z in accordance with Equation (13). The primary field is axial symmetric when the incline angle is zero but asymmetric when the incline is not zero, resulting in asymmetric distribution of the apparent resistivities.

Figure 8 shows the apparent resistivity of the two models at 1 Hz; the first and second rows in this figure correspond to anisotropic and isotropic models respectively, whereas the first to fifth columns correspond to Tx incline angles of −30°, −15°, 0°, 15° and 30° respectively. The data (Figure 8) show that the distribution of the apparent resistivity changes when the incline angle changes; the distributions of the anisotropic and isotropic models exhibit different behaviours for the same incline angle and the EM wave at 1 Hz is a non-plane wave.

(2) A single oblique Ty source. We also studied a further isotropic model for comparison. In this case, the conductivity of the 3D anisotropic anomaly was set at 0.0025 S/m; the apparent resistivities of these two models at 100 and 1 Hz are shown in Figures 9

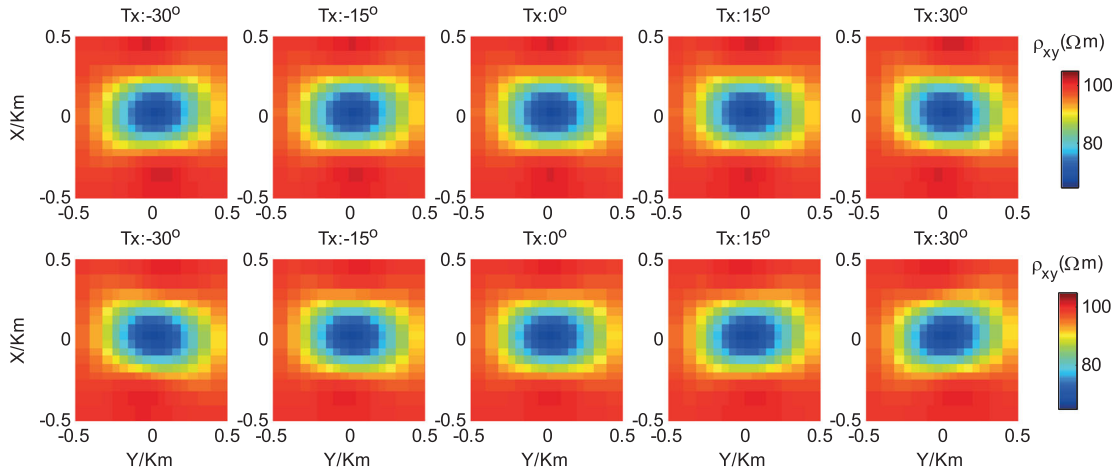

Figure 7. Apparent resistivity of an oblique Tx source at 100 Hz: (a) the first row corresponds to the anisotropic model; (b) the second row corresponds to the isotropic model.

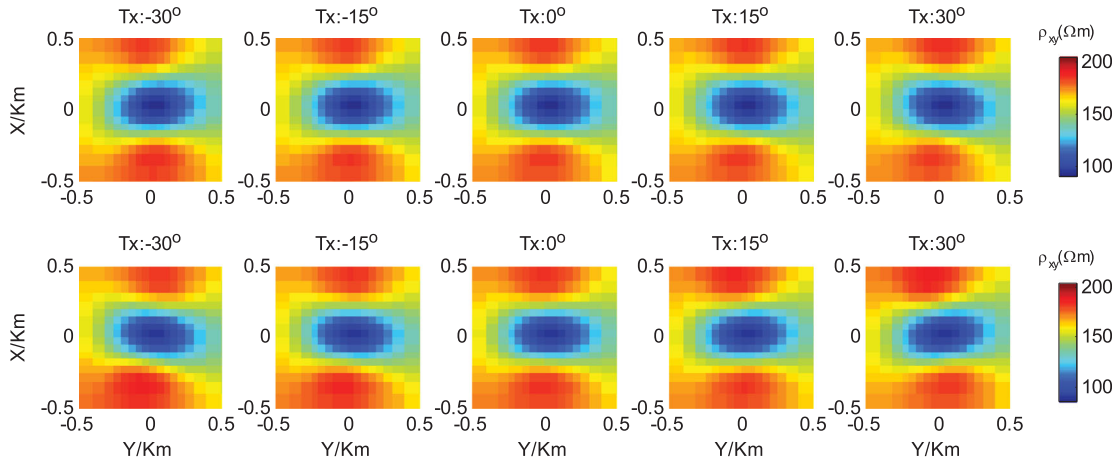

Figure 8. Apparent resistivity of the oblique Tx source at 1 Hz: (a) the first row corresponds to the anisotropic model; (b) the second row corresponds to the isotropic model.

and 10, respectively. The first row in these figures corresponds to the anisotropic model, whereas the second row corresponds to the isotropic model; the first to fifth columns correspond to Ty incline angles of −30°, −15°, 0°, 15° and 30° respectively. These figures show that the distribution of the apparent resistivity changes as the incline angles change; the anisotropic and isotropic models exhibit different apparent resistivity behaviours for the same incline angle.

Euler's angle changes

It is the case for both Tx and Ty sources that when one Euler's angle changes, the other two remain equal to zero. However, as only angle α_S changes when the other two remain equal zero is the same as the case that only angle α_L changes when the other two are equal to zero (Pek and Santos 2002; Xiao et al. 2018), therefore, the results of the latter case are not shown in this paper.

(1) A Tx source. The data in Figure 11 summarise apparent resistivity changes at different Euler's angles and a frequency of 100 Hz. The first and second rows correspond to angles α_S and α_D respectively, whereas the first to seventh columns correspond to angles of −90°, −60°, −30°, 0°, 30°, 60° and 90° respectively. The solid purple line used throughout the figures encapsulates angles with respect to the negative *y*-direction of −90°, −60°, −30°, 0°, 30°, 60° and 90° from left to right. Thus, as shown in Figure 11, the apparent resistivity changes when angle α_S changes and the purple line agrees with the direction of distribution for the lower apparent resistivity from left to right. This phenomenon occurs when one of the two principal conductivities in the xoy plane is larger than the background conductivity and the other is smaller. By contrast, apparent resistivity remains almost constant when angle α_D changes because the conductivity in the *x*-direction remains unchanged. In addition, the apparent resistivity when angle α_S is −90° is the same as that when angle α_S is 90° because their conductivities are the same. The apparent resistivity when angle α_S

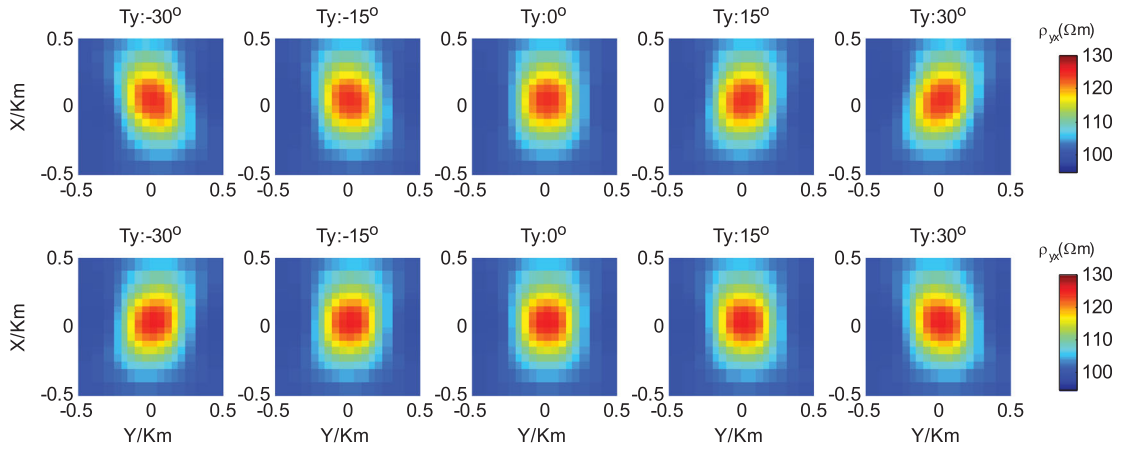

Figure 9. Apparent resistivity of the oblique Ty source at 100 Hz: (a) the first row corresponds to the anisotropic model; (b) the second row corresponds to the isotropic model.

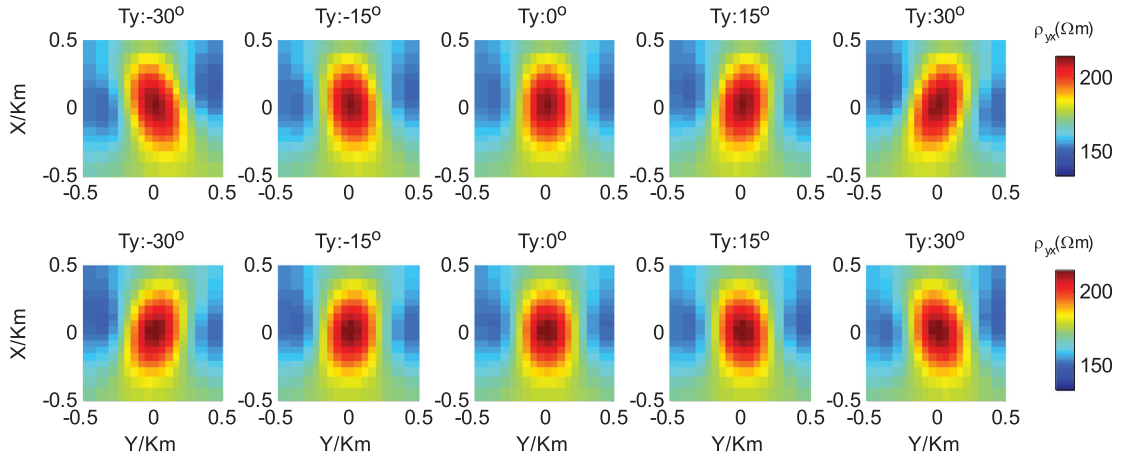

Figure 10. Apparent resistivity of the oblique Ty source at 1 Hz: (a) the first row corresponds to the anisotropic model; (b) the second row corresponds to the isotropic model.

is −60° runs counter to the value when angle α_S is 60°, and the same is true for angles of −30° and 30°.

Apparent resistivity values for different Euler's angles at 1 Hz are shown in Figure 12. The first row corresponds to angle α_S, and the second row to angle α_D; the first to seventh columns correspond to angles of −90°, −60°, −30°, 0°, 30°, 60° and 90° respectively. As shown in Figure 12, the EM wave at 1 Hz is non-planar; thus, like Figure 11, apparent resistivity changes when angle α_S changes, and the solid purple line agrees with the direction of distribution for the lower apparent resistivity. Similarly, apparent resistivity remains almost unchanged when angle α_D changes, whereas when angle α_S is −90° apparent resistivity is the same as when angle α_S is 90°. Finally, apparent resistivity when angle α_S is −60° runs counter to the value when angle α_S is 60°, and the same is true for angles of −30° and 30°.

(2) A Ty source. Apparent resistivity values for different Euler's angles at 100 and 1 Hz are shown in Figures 13 and 14 respectively. The first and second rows correspond to angles α_S and α_D respectively, whereas the first to seventh columns correspond to angles of −90°, −60°, −30°, 0°, 30°, 60° and 90° respectively. In both cases, apparent resistivity changes when angle α_S changes, and the solid purple line agrees with the direction of distribution for the lower apparent resistivity. It is also the case that apparent resistivity changes in concert with angle α_D; there are almost no apparent resistivity anomalies when angle α_D equals −90° or 90° because conductivity in the *x*-direction is 0.01 S/m and this remains unchanged when α_D is −90° or 90°. Similarly, apparent resistivity when angle α_S is −90° is the same as when α_S is 90°, but when this falls to −60° the results are counter to those when angle α_S is 60°, and the same is true for angles of −30° and 30°.

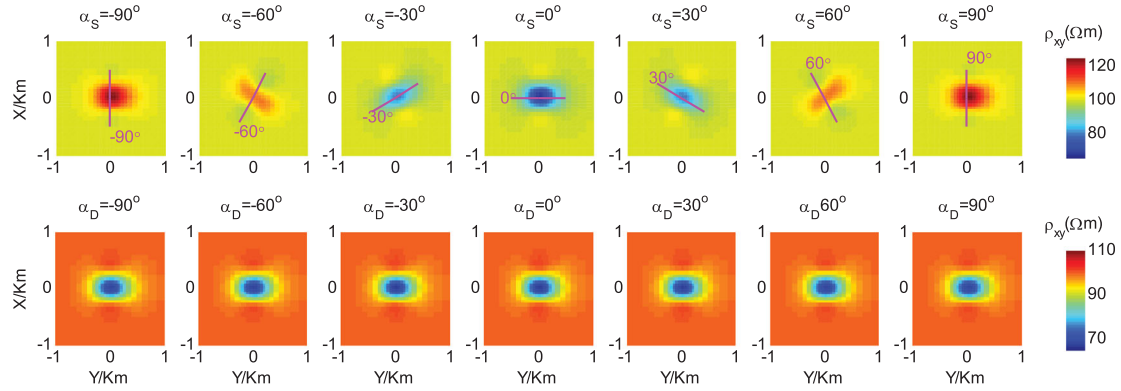

Figure 11. Apparent resistivity with different Euler's angles of the Tx source at 100 Hz.

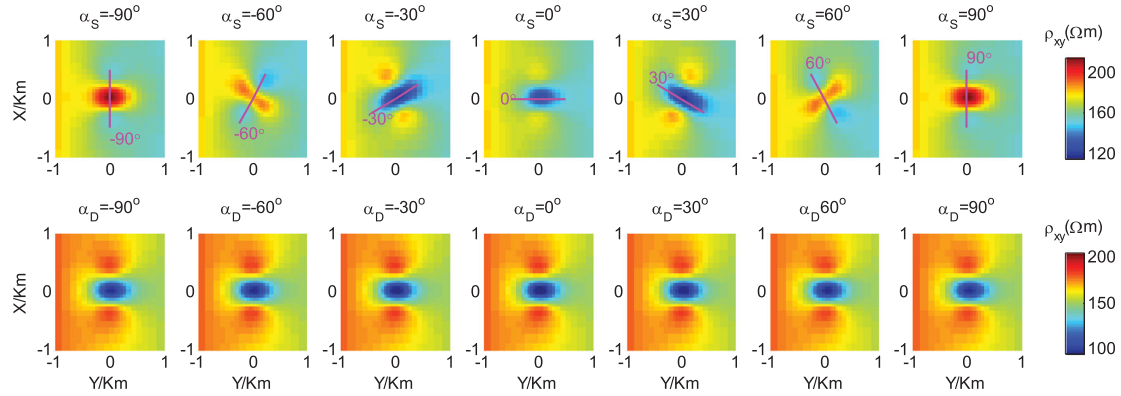

Figure 12. Apparent resistivity with different Euler's angles of the Tx source at 1 Hz.

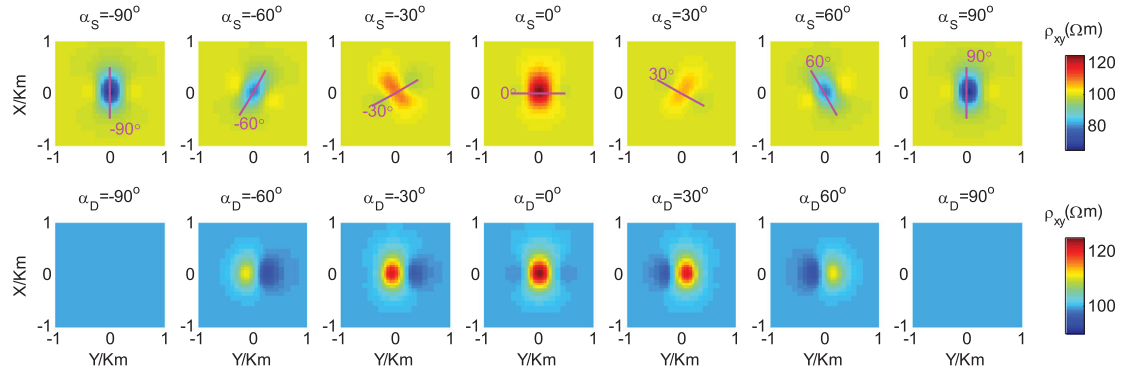

Figure 13. Apparent resistivity with different Euler's angles of the Ty source at 100 Hz.

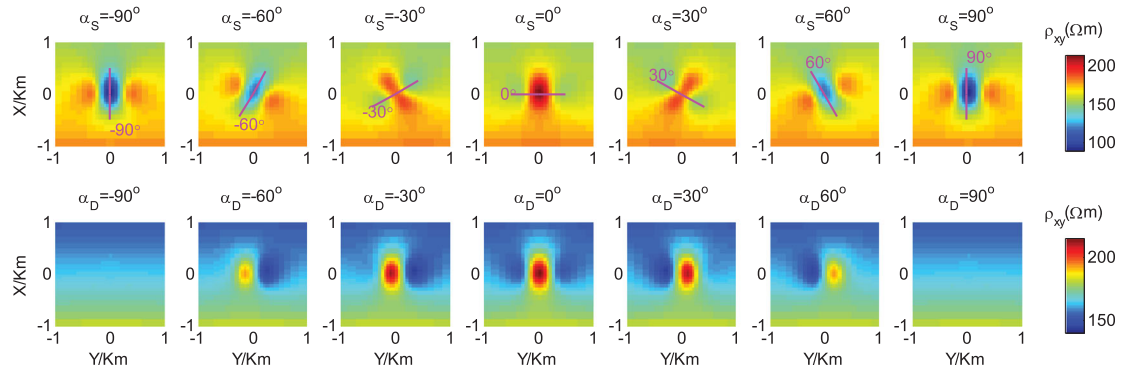

Figure 14. Apparent resistivity with different Euler's angles of the Ty source at 1 Hz.

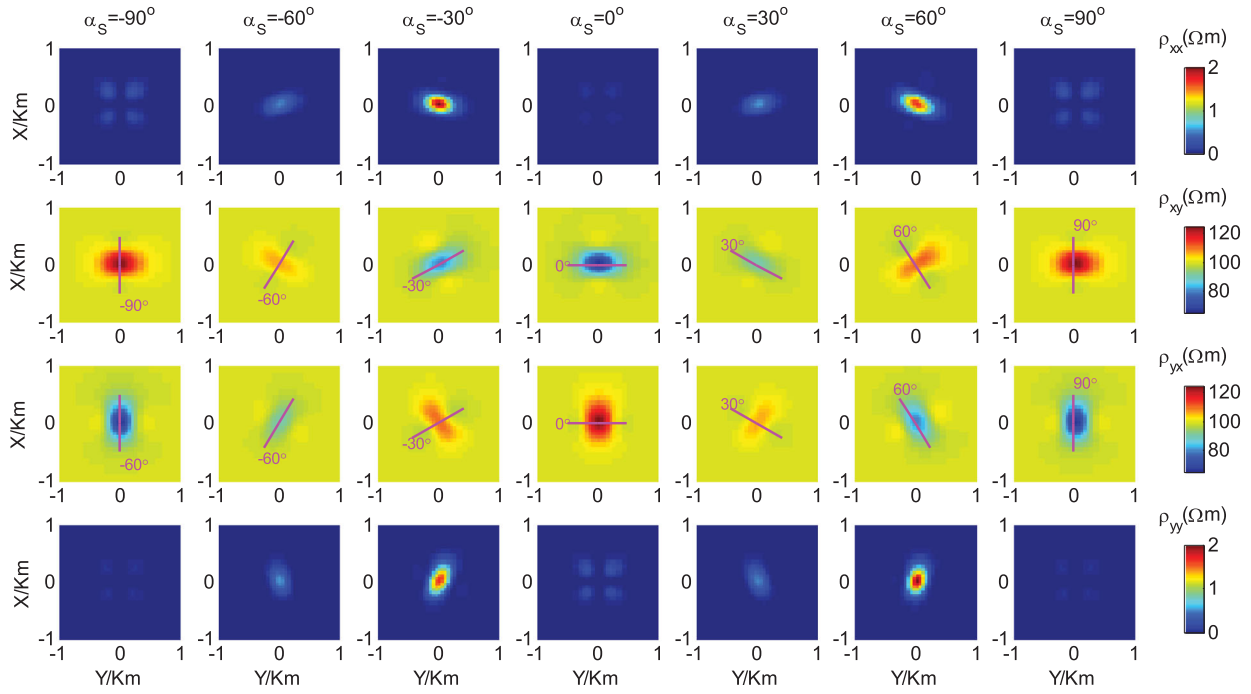

Figure 15. Apparent resistivity with different α_S angles of tensor source at 100 Hz.

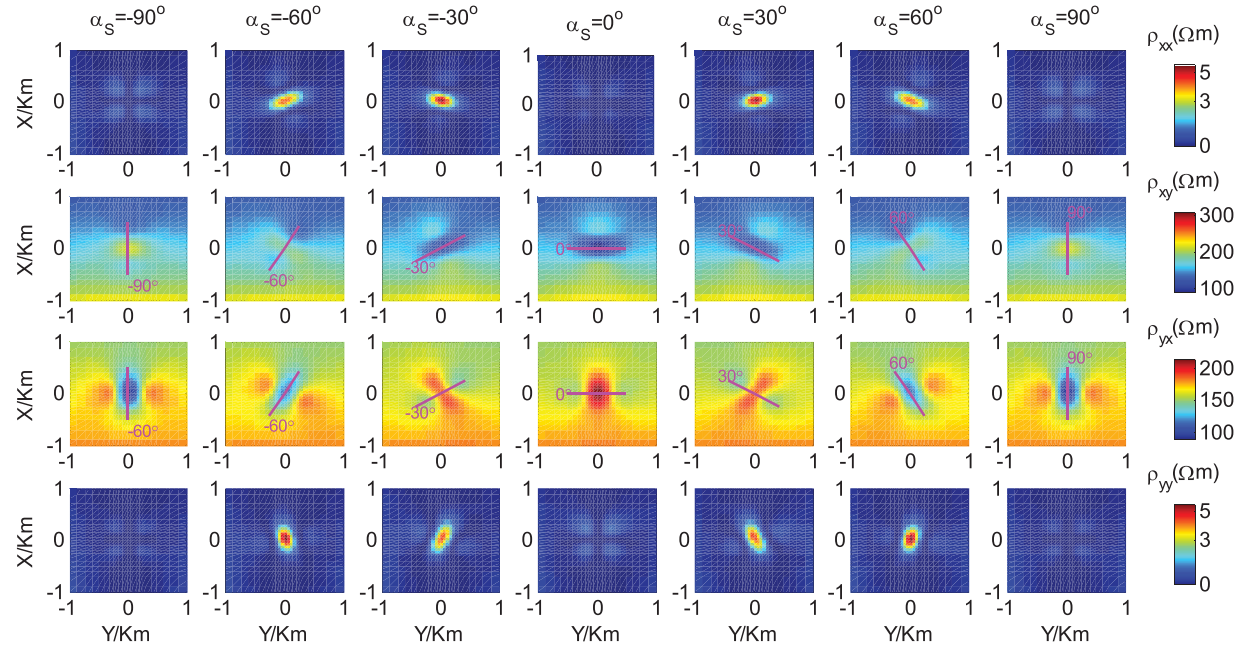

Figure 16. The apparent resistivity with different α_S angles of tensor source at 1 Hz.

Comparing the Tx source results with those from the Ty source reveals a large difference between the apparent resistivities of xy- and yx-modes; we therefore conclude that use of a single source for Tx or Ty in 3D anisotropic media is inappropriate.

Tensor source

Because we have shown that it is inappropriate to use a single source for 3D anisotropic media, a tensor source is studied in this section.

Simple 3D anisotropic model

This model is still used, as shown in Figure 4, and three principal conductivities of the anomaly are 0.04, 0.0025 and 0.01 S/m respectively; and the conductivity of the isotropic half-space remained set to 0.01 S/m.

(1) Angle α_S changes. The results in Figures 15 and 16 are for apparent resistivities of 100 and 1 Hz respectively. The first to fourth rows correspond to xx-, xy-, yx- and yy-mode apparent resistivities respectively,

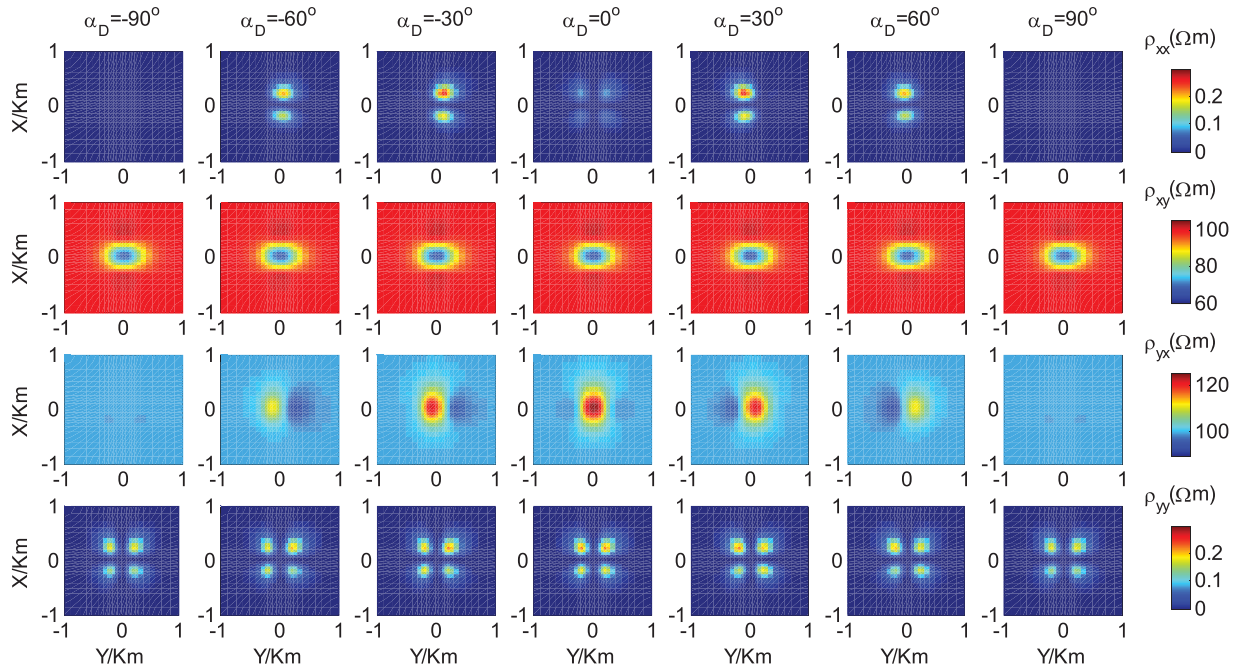

Figure 17. Apparent resistivity with different α_D angles of the tensor source at 100 Hz.

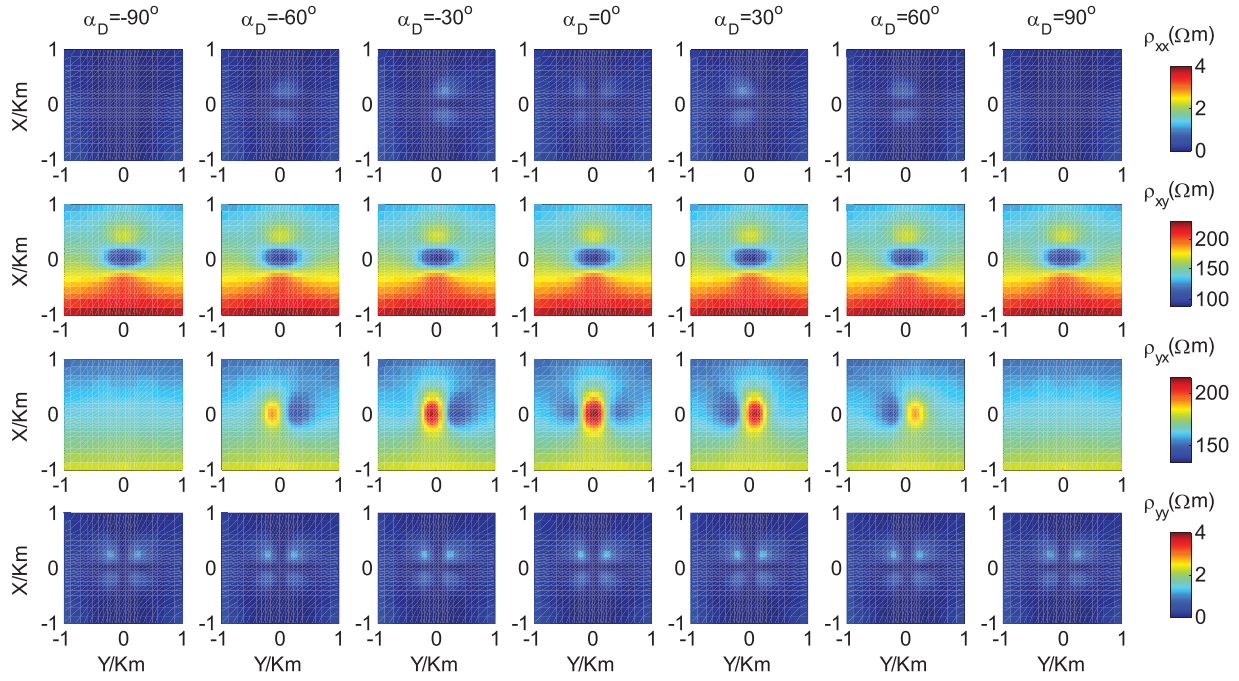

Figure 18. Apparent resistivity with different α_D angles of the tensor source at 1 Hz.

whereas the first to seventh columns from left to right correspond to α_S angles of −90°, −60°, −30°, 0°, 30°, 60° and 90° respectively. These results show that apparent resistivities for all four modes change in concert with α_S; in the case of xy- and yx-modes, the solid purple line agrees with the direction of the lower apparent resistivity from left to right respectively, whereas values when angle α_S is −90° are the same as those when α_S is 90°. The distribution of apparent resistivities when angle α_S is −60° also runs counter to the distribution when angle α_S is 60° and the same is true for angles of −30° and 30°. It is also clear that the EM wave at 100 Hz is similar to a plane wave case, although, the EM wave at 1 Hz is non-planar.

(2) Angle α_D changes. Apparent resistivities of 100 and 1 Hz are shown in Figures 17 and 18, respectively. The first to seventh columns from left to right correspond to α_D angles of −90°, −60°, −30°, 0°, 30°, 60° and 90° respectively, whereas the first to fourth rows correspond to the xx-, xy-, yx-, and yy-mode apparent resistivities respectively. The data presented in Figures 17 and 18 show that both xy- and yy-mode apparent resistivities remain almost unchanged when angle α_D changes because conductivity in the *x*-direction remains

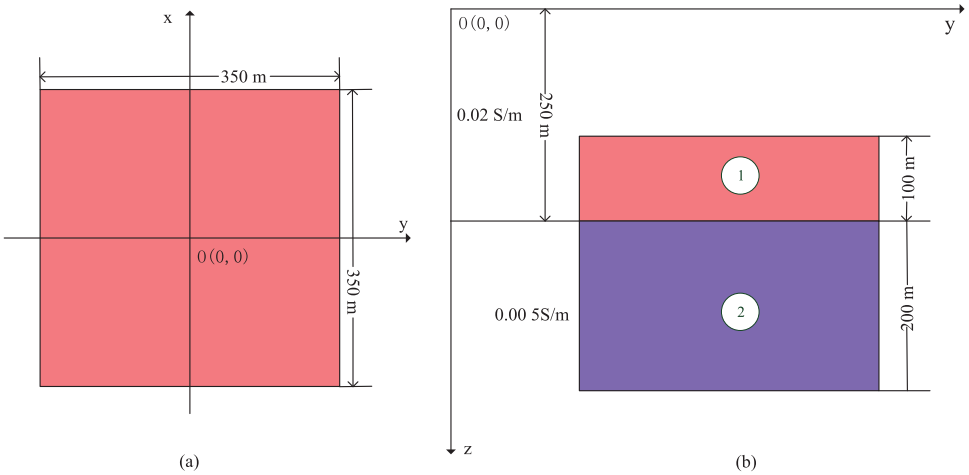

Figure 19. The synthetic model: (a) plan view; (b) section view.

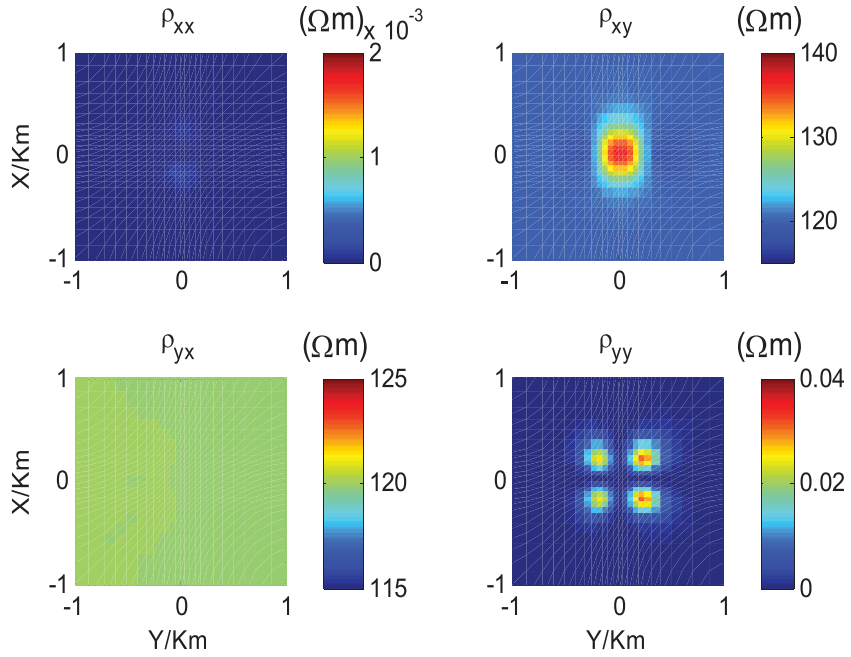

Figure 20. Apparent resistivities at 100 Hz.

constant as this angle varies. At the same time, both yx- and xx-mode apparent resistivities change when angle α_D varies; apparent resistivity values when angle α_D is $-90°$ are the same as those when α_D is 90° because their conductivities are identical. These data also show that the distribution of apparent resistivities when angle α_D is $-60°$ runs counter to that when α_D is 60°, and the same is true for angles of $-30°$ and 30°. Finally, both yx- and xx-mode apparent resistivities contain no anomalies when angle α_D is $-90°$ or 90° because the conductivity is in the *x*-direction is 0.01 S/m and this remains unchanged when angle α_D is $-90°$ or 90°.

Our analyses show that if a principal conductivity of the anomaly is in the *x*-direction, then both xy- and yy-mode apparent resistivities remain almost unchanged. However, because the *x*- and *y*-axes are interchangeable, yx- and xx-mode apparent resistivities remain almost unchanged if a principal conductivity of the anomaly is in the *y*-direction.

Synthetic models

The data in Figure 19 report a case when two 3D anisotropic anomalies are embedded in two-layered isotropic media. The first of these layers has a conductivity of 0.02 S/m with a thickness of 250 m, and the second has a conductivity of 0.005 S/m. The two 3D anisotropic anomalies are therefore presented; the ① anomaly embedded within the first layer with a top depth of 150 m has axial conductivities of 0.0025, 0.02 and 0.01 S/m respectively. The three Euler's angles in this case are all zero, and the dimensions of this anomaly are 350 m × 350 m × 100 m. Its counterpart, the ② anomaly, is embedded in the second layer and has a top depth of 250 m, three axial conductivities of

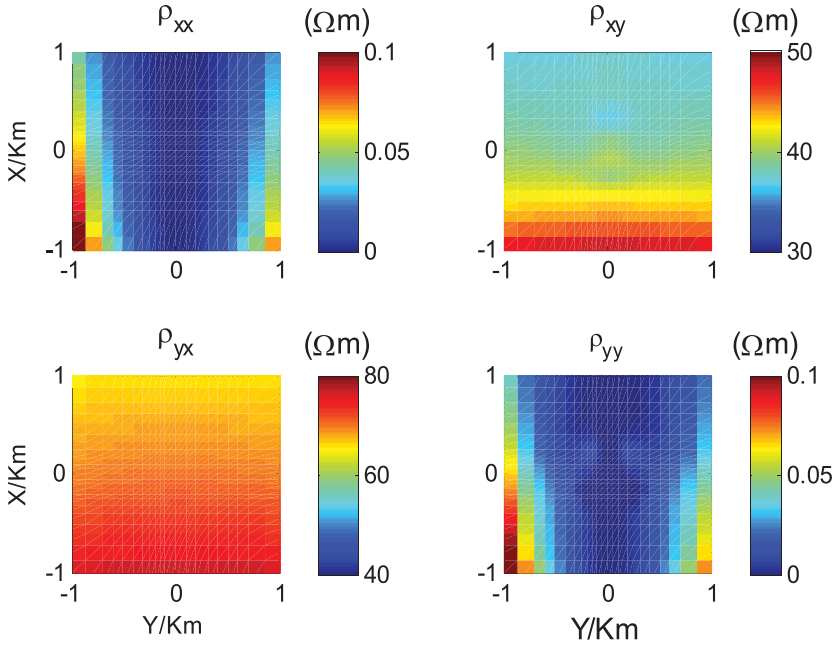

Figure 21. Apparent resistivities at 1 Hz.

0.04 0.005 and 0.01 S/m, three Euler's angles that are all zero and dimensions of 350 m × 350 m × 200 m.

Apparent resistivities at 100 and 1 Hz are shown in Figures 20 and 21, respectively. These data show that xy- and yy-mode apparent resistivities obviously contain anomalies but their yx- and xx-mode counterparts do not because the conductivity in the *y*-direction remains the same as that of both the first and second layers respectively. The results corroborate our earlier conclusions.

Conclusions

An edge-based FE algorithm is presented in this study to simulate the responses of CSAMT in 3D generalised anisotropic media. The accuracy of this approach was also validated by comparison with previous results; for the apparent resistivities and phase, it shows that the relative errors are all $<$ 1%. We also investigated the responses of both a single source and a tensor source under different conditions, leading to a number of important conclusions. We show that in the case of a single source, including oblique single Tx and Ty cases, the incline angle of the source exerts an influence on the responses and therefore cannot be ignored. We also show that in the case of an oblique single Tx source, if one principal conductivity of the anomaly is in the *x*-direction, then the apparent resistivity (xy-mode) remains almost the same; by contrast, for an oblique single Ty source, if one principal conductivity of the anomaly is in the *y*-direction, then the apparent resistivity (yx-mode) remains almost unchanged. We therefore argue that it is inappropriate to utilise a single source (Tx or Ty) for CSAMT in 3D anisotropic media. In the case of tensor source use, however, if a principal conductivity of the anomaly is in the *x*-direction then xy- and yy-mode apparent resistivities remain almost unchanged, but if a principal conductivity is in the *y*-direction then yx- and xx-mode apparent resistivities remain almost the same.

Acknowledgements

Thanks to Dr Kerry Key for his 1D CSEM modelling code. This study is co-funded by the National Key Research and Development Project of China (2016YFC0600301) and the National Natural Science Foundation of China (No. 41425017).

Disclosure statement

No potential conflict of interest was reported by the authors.

Funding

This study is co-funded by the National Key Research and Development Project of China (2016YFC0600301) and the National Natural Science Foundation of China (No. 41425017).

References

Ansari, S., and C.G. Farquharson. 2014. 3d finite-element forward modeling of electromagnetic data using vector and scalar potentials and unstructured grids. *Geophysics* 79: E149–E165. doi:10.1190/geo2013-0172.1.

Boerner, D.E., J.A. Wright, J.G. Thurlow, and L.E. Reed. 1993. Tensor CSAMT studies at the Buchans Mine in central Newfoundland. *Geophysics* 58: 12–19. doi:10.1190/1.1443342.

Cai, H., X. Hu, J. Li, M. Endo, and B. Xiong. 2017. Parallelized 3D CSEM modeling using edge-based finite element with total field formulation and unstructured mesh. *Computers & Geosciences* 99: 125–134. doi:10.1016/j.cageo.2016.11.009.

Cai, H., B. Xiong, M. Han, and M. Zhdanov. 2014. 3D controlled-source electromagnetic modeling in anisotropic medium using edge-based finite element method. *Computers & Geosciences* 73: 164–176. doi:10.1016/j.cageo.2014.09.008.

Di, Q., U. Martyn, and M. Wang. 2004. 2.5-D CSAMT modeling with finite element method over 2-D complex

earth media. *Chinese Journal of Geophysics (in Chinese)* 47: 825–829.

Evans, R.L., G. Hirth, K. Baba, D. Forsyth, A. Chave, and R. Mackie. 2005. Geophysical evidence from the MELT area for compositional controls on oceanic plates. *Nature* 437: 249–252. doi:10.1038/nature04014.

Farquharson, C.G., and M.P. Miensopust. 2011. Three-dimensional finite-element modelling of magnetotelluric data with a divergence correction. *Journal of Applied Geophysics* 75: 699–710. doi:10.1016/j.jappgeo.2011.09.025.

Fu, C., Q. Di, and Z. An. 2013. Application of the CSAMT method to groundwater exploration in a metropolitan environment. *Geophysics* 78: B201–B209. doi:10.1190/geo2012-0533.1.

Hu, Y., T. Li, C. Fan, D. Wang, and J. Li. 2015. Three-dimensional tensor controlled-source electromagnetic modeling based on the vector finite-element method. *Applied Geophysics* 12: 35–46. doi:10.1007/s11770-014-0469-1.

Hu, X., R. Peng, G. Wu, W. Wang, G. Huo, and B. Han. 2013. Mineral exploration using CSAMT data: application to Longmen region metallogenic belt, Guangdong Province, China. *Geophysics* 78: B111–B119. doi: 10.1190/geo2012-0115.1.

Jakobsen, M. and S. Tveit. 2018. Distorted Born iterative T-matrix method for inversion of CSEM data in anisotropic media. *Geophysical Journal International*. doi:10.1093/gji/ggy197

Jin, J.M. 2002. *The finite element method in electromagnetics*. 2nd ed. New York: John Wiley and Sons.

Key, K. 2009. 1D inversion of multicomponent, multifrequency marine CSEM data: Methodology and synthetic studies for resolving thin resistive layers. *Geophysics* 74: F9–F20. doi:10.1190/1.3058434.

Kong, F.N., S.E. Johnstad, T. Røsten, and H. Westerdahl. 2008. A 2.5 D finite-element-modeling difference method for marine CSEM modeling in stratified anisotropic media. *Geophysics* 73: F9–F19. doi:10.1190/1.2819691.

Kong, W., C. Lin, H. Tan, M. Peng, T. Tong, and M. Wang. 2018. The effects of 3D electrical anisotropy on magnetotelluric responses: synthetic case studies. *Journal of Environmental and Engineering Geophysics* 23: 61–75. doi:10.2113/JEEG23.1.61.

Li, J., C.G. Farquharson, and X. Hu. 2016. 3D vector finite-element electromagnetic forward modeling for large loop sources using a total-field algorithm and unstructured tetrahedral grids. *Geophysics* 82: E1–E16. doi.org/10.1190/geo2016-0004.1.

Li, X., and L.B. Pedersen. 1992. Controlled-source tensor magnetotelluric responses of a layered earth with azimuthal anisotropy. *Geophysical Journal International* 111: 91–103. doi:10.1111/j.1365-246X.1992.tb00557.x.

Lin, C., H. Tan, Q. Shu, T. Tong, and J. Tan. 2012. Three-dimensional conjugate gradient inversion of CSAMT data. *Chinese Journal of Geophysics (in Chinese)* 55: 3829–3838. doi:10.6038/j.issn.0001-5733.2012.11.030.

Lu, X., M. Unsworth, and J. Booker. 1999. Rapid relaxation inversion of CSAMT data. *Geophysical Journal International* 138: 381–392. doi:10.1046/j.1365-246X.1999.00871.x.

McMillan, M.S., and D.W. Oldenburg. 2014. Cooperative constrained inversion of multiple electromagnetic data sets cooperative EM inversion. *Geophysics* 79: B173–B185. doi:10.1190/geo2014-0029.1.

Mitsuhata, Y., and T. Uchida. 2004. 3D magnetotelluric modeling using the T-Ω finite-element method. *Geophysics* 69 no. 1: 108–119. doi.org/10.1190/1.1649380.

Newman, G.A., M. Commer, and J.J. Carazzone. 2010. Imaging CSEM data in the presence of electrical anisotropy. *Geophysics* 75: F51–F61. doi:10.1190/1.3295883.

Pedrera, A., S. Martos-Rosillo, J. Galindo-Zaldívar, M. Rodríguez-Rodríguez, J. Benavente, J.F. Martín-Rodríguez, and M.I. Zúñiga-López. 2016. Unravelling aquifer-wetland interaction using CSAMT and gravity methods: the Mollina-Camorra aquifer and the Fuente de Piedra playa-lake, southern Spain. *Journal of Applied Geophysics* 129: 17–27.

Pek, J., and F.A. Santos. 2002. Magnetotelluric impedances and parametric sensitivities for 1-D anisotropic layered media. *Computers & Geosciences* 28: 939–950. doi:10.1016/S0098-3004(02)00014-6.

Puzyrev, V., J. Koldan, J. de la Puente, G. Houzeaux, M. Vázquez, and J.M. Cela. 2013. A parallel finite-element method for three-dimensional controlled-source electromagnetic forward modelling. *Geophysical Journal International* 193: 678–693. doi:10.1093/gji/ggt027.

Ren, Z.Y., T. Kalscheuer, S. Greenhalgh, and H. Maurer. 2013. A goal-oriented adaptive finite-element approach for plane wave 3-D electromagnetic modeling. *Geophysical Journal International* 194 no. 2: 700–718. doi:10.1093/gji/ggt154.

Routh, P.S., and D.W. Oldenburg. 1999. Inversion of controlled source audio-frequency imagnetotellurics data for a horizontally layered earth. *Geophysics* 64: 1689–1697. doi:10.1190/1.1444673.

Unsworth, M.J., X. Lu, and M. Don Watts. 2000. CSAMT exploration at Sellafield: Characterization of a potential radioactive waste disposal site. *Geophysics* 65 no. 4: 1070–1079.

Wang, F., J.P. Morten, and K. Spitzer. 2018. Anisotropic three-dimensional inversion of CSEM data using finite-element techniques on unstructured grids. *Geophysical Journal International* 213: 1056–1072. doi:10.1093/gji/ggy029.

Wang, K., and H. Tan. 2017. Research on the forward modeling of controlled-source audio-frequency magnetotellurics in three-dimensional axial anisotropic media. *Journal of Applied Geophysics* 146: 27–36. doi:10.1016/j.jappgeo.2017.08.007.

Wang, K., H. Tan, C. Lin, J. Yuan, C. Wang, and J. Tang. 2017a. Three-dimensional tensor controlled-source audio-frequency magnetotelluric inversion using LBFGS. *Exploration Geophysics*. doi:10.1071/EG16079.

Wang, K.P., H.D. Tan, and T. Wang. 2017b. 2D joint inversion of CSAMT and magnetic data based on cross-gradient theory. *Applied Geophysics* 14: 279–290. doi:10.1007/s11770-017-0615-z.

Wang, R., C.C. Yin, M.Y. Wang, and Q.Y. Di. 2015. Laterally constrained inversion for CSAMT data interpretation. *Journal of Applied Geophysics* 121: 63–70. doi:10.1016/j.jappgeo.2015.07.009.

Wang, T., K. Wang, and H. Tan. 2017c. Forward modeling and inversion of tensor CSAMT in 3D anisotropic media. *Applied Geophysics* 14: 590–605. doi:10.1007/s11770-017-0644-7.

Wannamaker, P.E. 1997. Tensor CSAMT survey over the Sulphur Springs thermal area, Valles Caldera, New Mexico, United States of America, Part I: Implications for structure of the western caldera. *Geophysics* 62: 451–465. doi:10.1190/1.1444156.

Xiao, T., Y. Liu, Y. Wang, and L.Y. Fu. 2018. Three-dimensional magnetotelluric modeling in anisotropic media using edge-based finite element method. *Journal of Applied Geophysics* 149: 1–9. doi:10.1016/j.jappgeo.2017.12.009.

Xu, S.Z. 1994. *The finite element methods in geophysics*. Beijing, China: Science Press.

Yin, C. 2000. Geoelectrical inversion for a one-dimensional anisotropic model and inherent non-uniqueness. *Geophysical Journal International* 140: 11–23. doi:10.1046/j.1365-246x.2000.00974.x.

Yin, C.C., F. Ben, Y.H. Liu, W. Huang, and J. Cai. 2014. MCSEM 3Dmodeling for arbitrarily anisotropic media. *Chinese Journal of Geophysics (in Chinese)* 57: 4110–4122. doi:10.6038/cjg20141222.

Younis, A., G. El-Qady, M. Abd Alla, M. Abdel Zaher, A. Khalil, M. Al Ibiary, and A. Saraev. 2015. AMT and CSAMT methods for hydrocarbon exploration at nile delta, egypt. *Arabian Journal of Geosciences* 8: 1965–1975. doi:10.1007/s12517-014-1354-6.

Appendix A

(1)

$$\nabla\times\mathbf{N}\cdot\nabla\times\mathbf{N}=\nabla\times\sum_{i=1}^{4}(\mathbf{N}_{xi}+\mathbf{N}_{yi}+\mathbf{N}_{zi})\cdot\nabla\times\sum_{j=1}^{4}(\mathbf{N}_{xj}+\mathbf{N}_{yj}+\mathbf{N}_{zj})=\sum_{i=1}^{4}\sum_{j=1}^{4}\times\begin{pmatrix}\left[\frac{\partial \mathrm{N}_{xi}}{\partial y}\frac{\partial \mathbf{N}_{xj}}{\partial y}+\frac{\partial \mathbf{N}_{xi}}{\partial z}\frac{\partial \mathbf{N}_{xj}}{\partial z}\right] & \left[-\frac{\partial \mathbf{N}_{xi}}{\partial y}\frac{\partial \mathbf{N}_{yj}}{\partial x}\right] & \left[-\frac{\partial \mathbf{N}_{xi}}{\partial z}\frac{\partial \mathbf{N}_{zj}}{\partial x}\right]\\ \left[-\frac{\partial \mathbf{N}_{yi}}{\partial x}\frac{\partial \mathbf{N}_{xj}}{\partial y}\right] & \left[\frac{\partial \mathbf{N}_{yi}}{\partial x}\frac{\partial \mathbf{N}_{yj}}{\partial x}+\frac{\partial \mathbf{N}_{yi}}{\partial z}\frac{\partial \mathbf{N}_{yj}}{\partial z}\right] & \left[-\frac{\partial \mathbf{N}_{yi}}{\partial z}\frac{\partial \mathbf{N}_{zj}}{\partial y}\right]\\ \left[-\frac{\partial \mathbf{N}_{zi}}{\partial x}\frac{\partial \mathbf{N}_{xj}}{\partial z}\right] & \left[-\frac{\partial \mathbf{N}_{zi}}{\partial y}\frac{\partial \mathbf{N}_{yj}}{\partial z}\right] & \left[\frac{\partial \mathbf{N}_{zi}}{\partial x}\frac{\partial \mathbf{N}_{zj}}{\partial x}+\frac{\partial \mathbf{N}_{zi}}{\partial y}\frac{\partial \mathbf{N}_{zj}}{\partial y}\right]\end{pmatrix}=\mathbf{K}_{1e}=\begin{bmatrix}\mathbf{K}_{1e}^{xx} & \mathbf{K}_{1e}^{xy} & \mathbf{K}_{1e}^{xz}\\ \mathbf{K}_{1e}^{yx} & \mathbf{K}_{1e}^{yy} & \mathbf{K}_{1e}^{yz}\\ \mathbf{K}_{1e}^{zx} & \mathbf{K}_{1e}^{zy} & \mathbf{K}_{1e}^{zz}\end{bmatrix} \tag{A1}$$

where

$$\mathbf{K}_{1e}^{xx}=\int_e\left[\left(\frac{\partial N_{xi}}{\partial y}\frac{\partial N_{xj}}{\partial y}+\frac{\partial N_{xi}}{\partial z}\frac{\partial N_{xj}}{\partial z}\right)\right]\mathrm{d}x\mathrm{d}y\mathrm{d}z=\frac{ac}{6b}\begin{bmatrix}2&-2&1&-1\\-2&2&-1&1\\1&-1&2&-2\\-1&1&-2&2\end{bmatrix}+\frac{ab}{6c}\begin{bmatrix}2&1&-2&-1\\1&2&-1&-2\\-2&-1&2&1\\-1&-2&1&2\end{bmatrix} \tag{A2}$$

$$\mathbf{K}_{1e}^{xy}=\int_e\left(-\frac{\partial N_{xi}}{\partial y}\frac{\partial N_{yj}}{\partial x}\right)\mathrm{d}x\mathrm{d}y\mathrm{d}z=-\frac{c}{6}\begin{bmatrix}2&1&-2&-1\\-2&-1&2&1\\1&2&-1&-2\\-1&-2&1&2\end{bmatrix} \tag{A3}$$

$$\mathbf{K}_{1e}^{xz}=\int_e\left(-\frac{\partial N_{xi}}{\partial z}\frac{\partial N_{zj}}{\partial x}\right)\mathrm{d}x\mathrm{d}y\mathrm{d}z=-\frac{b}{6}\begin{bmatrix}2&-2&1&-1\\1&-1&2&-2\\-2&2&-1&1\\-1&1&-2&2\end{bmatrix} \tag{A4}$$

$$\mathbf{K}_{1e}^{yx}=\int_e\left(-\frac{\partial N_{yi}}{\partial x}\frac{\partial N_{xj}}{\partial y}\right)\mathrm{d}x\mathrm{d}y\mathrm{d}z=-\frac{c}{6}\begin{bmatrix}2&-2&1&-1\\1&-1&2&-2\\-2&2&-1&1\\-1&1&-2&2\end{bmatrix} \tag{A5}$$

$$\mathbf{K}_{1e}^{yy}=\int_e\left(\frac{\partial N_{yi}}{\partial x}\frac{\partial N_{yj}}{\partial x}+\frac{\partial N_{yi}}{\partial z}\frac{\partial N_{yj}}{\partial z}\right)\mathrm{d}x\mathrm{d}y\mathrm{d}z=\frac{bc}{6a}\begin{bmatrix}2&1&-2&-1\\1&2&-1&-2\\-2&-1&2&1\\-1&-2&1&2\end{bmatrix}+\frac{ab}{6c}\begin{bmatrix}2&-2&1&-1\\-2&2&-1&1\\1&-1&2&-2\\-1&1&-2&2\end{bmatrix} \tag{A6}$$

$$\mathbf{K}_{1e}^{yz}=\int_e\left(-\frac{\partial N_{yi}}{\partial z}\frac{\partial N_{zj}}{\partial y}\right)\mathrm{d}x\mathrm{d}y\mathrm{d}z=-\frac{a}{6}\begin{bmatrix}2&1&-2&-1\\-2&-1&2&1\\1&2&-1&-2\\-1&-2&1&2\end{bmatrix} \tag{A7}$$

$$\mathbf{K}_{1e}^{zx}=\int_e\left(-\frac{\partial N_{zi}}{\partial x}\frac{\partial N_{xj}}{\partial z}\right)\mathrm{d}x\mathrm{d}y\mathrm{d}z=-\frac{b}{6}\begin{bmatrix}2&1&-2&-1\\-2&-1&2&1\\1&2&-1&-2\\-1&-2&1&2\end{bmatrix} \tag{A8}$$

$$\mathbf{K}_{1e}^{zy}=\int_e\left(-\frac{\partial N_{zi}}{\partial y}\frac{\partial N_{yj}}{\partial z}\right)\mathrm{d}x\mathrm{d}y\mathrm{d}z=-\frac{b}{6}\begin{bmatrix}2&1&-2&-1\\-2&-1&2&1\\1&2&-1&-2\\-1&-2&1&2\end{bmatrix} \tag{A9}$$

$$\mathbf{K}_{1e}^{zz}=\int_e\left(\frac{\partial N_{zi}}{\partial x}\frac{\partial N_{zj}}{\partial x}+\frac{\partial N_{zi}}{\partial y}\frac{\partial N_{zj}}{\partial y}\right)\mathrm{d}x\mathrm{d}y\mathrm{d}z=\frac{bc}{6a}\begin{bmatrix}2&-2&1&-1\\-2&2&-1&1\\1&-1&2&-2\\-1&1&-2&2\end{bmatrix}+\frac{ac}{6b}\begin{bmatrix}2&1&-2&-1\\1&2&-1&-2\\-2&-1&2&1\\-1&-2&1&2\end{bmatrix} \tag{A10}$$

(2)

$$i\omega\mu_0\tilde{\sigma}\mathbf{N}\cdot\mathbf{N} = i\omega\mu_0\sum_{i=1}^{4}\sum_{j=1}^{4} \times\left\{\begin{bmatrix} N_{x,i} & 0 & 0\\ 0 & N_{z,i} & 0\\ 0 & 0 & N_{z,i}\end{bmatrix} \begin{bmatrix}\sigma_{xx} & \sigma_{xy} & \sigma_{xz}\\ \sigma_{yx} & \sigma_{yy} & \sigma_{yz}\\ \sigma_{zx} & \sigma_{zy} & \sigma_{zz}\end{bmatrix}\begin{bmatrix} N_{x,j} & 0 & 0\\ 0 & N_{z,j} & 0\\ 0 & 0 & N_{z,j}\end{bmatrix}\right\}$$

$$= \mathbf{K}_{2e} = i\omega\mu_0\begin{bmatrix}\sigma_{xx}\mathbf{K}_{2e}^{xx} & \sigma_{xy}\mathbf{K}_{2e}^{xy} & \sigma_{xz}\mathbf{K}_{2e}^{xz}\\ \sigma_{yx}\mathbf{K}_{2e}^{yx} & \sigma_{yy}\mathbf{K}_{2e}^{yy} & \sigma_{yz}\mathbf{K}_{2e}^{yz}\\ \sigma_{zx}\mathbf{K}_{2e}^{zx} & \sigma_{zy}\mathbf{K}_{2e}^{zy} & \sigma_{zz}\mathbf{K}_{2e}^{zz}\end{bmatrix} \tag{A11}$$

where

$$\mathbf{K}_{2e}^{xx} = i\omega\mu\int_e N_{xj}N_{xi}\mathrm{d}x\mathrm{d}y\mathrm{d}z = i\omega\mu\frac{abc}{36}\begin{bmatrix}4 & 2 & 2 & 1\\ 2 & 4 & 1 & 2\\ 2 & 1 & 4 & 2\\ 1 & 2 & 2 & 4\end{bmatrix} \tag{A12}$$

$$\mathbf{K}_{2e}^{xy} = i\omega\mu\int_e N_{xj}N_{yi}\mathrm{d}x\mathrm{d}y\mathrm{d}z = i\omega\mu\frac{abc}{24}\begin{bmatrix}2 & 1 & 2 & 1\\ 2 & 1 & 2 & 1\\ 1 & 2 & 1 & 2\\ 1 & 2 & 1 & 2\end{bmatrix} \tag{A13}$$

$$\mathbf{K}_{2e}^{xz} = i\omega\mu\int_e N_{xj}N_{zi}\mathrm{d}x\mathrm{d}y\mathrm{d}z = i\omega\mu\frac{abc}{24}\begin{bmatrix}2 & 2 & 1 & 1\\ 1 & 1 & 2 & 2\\ 2 & 2 & 1 & 1\\ 1 & 1 & 2 & 2\end{bmatrix} \tag{A14}$$

$$\mathbf{K}_{2e}^{yx} = i\omega\mu\int_e N_{yj}N_{xi}\mathrm{d}x\mathrm{d}y\mathrm{d}z = i\omega\mu\frac{abc}{24}\begin{bmatrix}2 & 2 & 1 & 1\\ 1 & 1 & 2 & 2\\ 2 & 2 & 1 & 1\\ 1 & 1 & 2 & 2\end{bmatrix} \tag{A15}$$

$$\mathbf{K}_{2e}^{yy} = i\omega\mu\int_e N_{yj}N_{yi}\mathrm{d}x\mathrm{d}y\mathrm{d}z = i\omega\mu\frac{abc}{36}\begin{bmatrix}4 & 2 & 2 & 1\\ 2 & 4 & 1 & 2\\ 2 & 1 & 4 & 2\\ 1 & 2 & 2 & 4\end{bmatrix} \tag{A16}$$

$$\mathbf{K}_{2e}^{yz} = i\omega\mu\int_e N_{yj}N_{zi}\mathrm{d}x\mathrm{d}y\mathrm{d}z = i\omega\mu\frac{abc}{24}\begin{bmatrix}2 & 1 & 2 & 1\\ 2 & 1 & 2 & 1\\ 1 & 2 & 1 & 2\\ 1 & 2 & 1 & 2\end{bmatrix} \tag{A17}$$

$$\mathbf{K}_{2e}^{zx} = i\omega\mu\int_e N_{zj}N_{xi}\mathrm{d}x\mathrm{d}y\mathrm{d}z = i\omega\mu\frac{abc}{24}\begin{bmatrix}2 & 1 & 2 & 1\\ 2 & 1 & 2 & 1\\ 1 & 2 & 1 & 2\\ 1 & 2 & 1 & 2\end{bmatrix} \tag{A18}$$

$$\mathbf{K}_{2e}^{zy} = i\omega\mu\int_e N_{zj}N_{yi}\mathrm{d}x\mathrm{d}y\mathrm{d}z = i\omega\mu\frac{abc}{24}\begin{bmatrix}2 & 2 & 1 & 1\\ 1 & 1 & 2 & 2\\ 2 & 2 & 1 & 1\\ 1 & 1 & 2 & 2\end{bmatrix} \tag{A19}$$

$$\mathbf{K}_{2e}^{zz} = i\omega\mu\int_e N_{zj}N_{zi}\mathrm{d}x\mathrm{d}y\mathrm{d}z = i\omega\mu\frac{abc}{36}\begin{bmatrix}4 & 2 & 2 & 1\\ 2 & 4 & 1 & 2\\ 2 & 1 & 4 & 2\\ 1 & 2 & 2 & 4\end{bmatrix} \tag{A20}$$

(3)

$$i\omega\mu_0\tilde{\sigma}^a\mathbf{N}\cdot\mathbf{N} = i\omega\mu_0\sum_{i=1}^{4}\sum_{j=1}^{4} \times\left\{\begin{bmatrix} N_{xi} & \mathbf{0} & \mathbf{0}\\ \mathbf{0} & N_{yi} & \mathbf{0}\\ \mathbf{0} & \mathbf{0} & N_{zi}\end{bmatrix} \begin{bmatrix}\sigma_{xx}^a & \sigma_{xy}^a & \sigma_{xz}^a\\ \sigma_{yx}^a & \sigma_{yy}^a & \sigma_{yz}^a\\ \sigma_{zx}^a & \sigma_{zy}^a & \sigma_{zz}^a\end{bmatrix}\begin{bmatrix} N_{xi}N_{xj} & \mathbf{0} & \mathbf{0}\\ \mathbf{0} & N_{yi}N_{yj} & \mathbf{0}\\ \mathbf{0} & \mathbf{0} & N_{zi}N_{zj}\end{bmatrix}\right\}$$

$$= \mathbf{K}_{3e} = i\omega\mu_0\begin{bmatrix}\sigma_{xx}^a\mathbf{K}_{3e}^{xx} & \sigma_{xy}^a\mathbf{K}_{3e}^{xy} & \sigma_{xz}^a\mathbf{K}_{3e}^{xz}\\ \sigma_{yx}^a\mathbf{K}_{3e}^{yx} & \sigma_{yy}^a\mathbf{K}_{3e}^{yy} & \sigma_{yz}^a\mathbf{K}_{3e}^{yz}\\ \sigma_{zx}^a\mathbf{K}_{3e}^{zx} & \sigma_{zy}^a\mathbf{K}_{3e}^{zy} & \sigma_{zz}^a\mathbf{K}_{3e}^{zz}\end{bmatrix} \tag{A21}$$

It is similar to $\mathbf{K}_{2e}$.